How Does an Air Film Evolve into a Bubble During Drop Impact?

Ji San Lee,[1] Byung Mook Weon,[1,*] Jung Ho Je,[1,†] and Kamel Fezzaa[2]

[1]X-ray Imaging Center, Department of Materials Science and Engineering, Pohang University of Science and Technology, San 31, Hyoja-dong, Pohang 790-784, Korea

[2]X-ray Science Division, Advanced Photon Source, Argonne National Laboratory, 9700 South Cass Avenue, Argonne, Illinois 60439, USA

(Received 7 August 2012; revised manuscript received 14 September 2012; published 13 November 2012)

When a liquid drop impacts a solid surface, air is generally entrapped underneath. Using ultrafast x-ray phase-contrast imaging, we directly visualized the profile of an entrapped air film and its evolution into a bubble during drop impact. We identified a complicated evolution process that consists of three stages: inertial retraction of the air film, contraction of the top air surface into a bubble, and pinch-off of a daughter droplet inside the bubble. Energy transfer during retraction drives the contraction and pinch-off of a daughter droplet. The wettability of the solid surface affects the detachment of the bubble, suggesting a method for bubble elimination in many drop-impact applications.

DOI: 10.1103/PhysRevLett.109.204501 PACS numbers: 47.55.D−, 47.55.db, 47.55.dr, 68.37.Yz

Introduction.—A liquid drop may spread on, splash onto, break up on, or bounce off of a solid surface when it impacts that surface, depending on the conditions associated with the liquid and solid, such as drop size, impact velocity, surface tension, viscosity, wettability, and roughness [1,2]. Interestingly, the surrounding air was found to significantly influence the drop impact process; for example, reducing the ambient air pressure can suppress splashing [3]. To understand the role of air in this process, several theoretical and experimental studies have been conducted in recent years [4–14]. Consensus is that an air film entrapped between a falling drop and a solid substrate critically affects the impact process and its outcome. Air entrapment is induced by a local pressure maximum right under the drop, which leads to the formation of a dimple and, thus, a liquid-solid contact ring, which was suggested by theoretical calculations [4,5,9] and then experimentally confirmed [10–13]. Due to minimization of surface energy, the air film must eventually evolve into a spherical bubble, as illustrated in Fig. 1(a). In fact, such bubbles have been observed [15–18]. However, the detailed evolution of an air film into a bubble is not clearly understood.

To investigate this evolution, it is necessary to visualize in real time the dynamics of an entrapped air film inside a liquid drop. This is a very challenging task with conventional visible-light imaging methods because they provide very limited information due to large reflection and scattering effects [7,18]. Moreover, interferometry [10,11,13] and total internal-reflection microscopy [12] can offer information on air thickness but cannot be used to track morphological changes of the air film in the vertical direction. To visualize the evolution of an air film into a bubble, we adopted a new technique based on x-ray phase-contrast imaging [Fig. 1(b)] [19,20], which enables the tracking of dynamic changes in air-liquid interfaces in real time. The excellent coherent nature of synchrotron x rays strongly enhances the phase contrast of air-liquid interfaces with sharp black and white fringes [19–21], despite being placed in a thick liquid medium [22,23].

In this work, we used ultrafast x-ray phase-contrast imaging to show that the evolution of an air film to a bubble occurs through a complicated, sequential process. The evolution consists of three stages: inertial retraction of the air film, contraction of the top air surface into a bubble, and pinch-off of a daughter droplet in the bubble. A series of ultrafast snapshots with an interval of 3.68 μs enabled us to clearly and quantitatively analyze detailed dynamics based on the tracking of morphological changes. Two important dynamic features were found: (i) the generation of the daughter droplet inside the bubble, which can be explained by energy transfer, and (ii) the detachment of the resultant bubble, which can be explained by solid wettability. Interestingly, bubble detachment may be a feasible way to eliminate bubbles in many drop-impact applications.

Experiments.—The experiments were conducted at the XSD 32-ID undulator beam line of the Advanced Photon Source, Argonne National Laboratory to achieve the high spatial and temporal resolution required for this experiment from an intense white (full energy spectrum) x-ray beam with a peak irradiance of $\sim 10^{14}$ ph/s/mm^2/0.1% bw [20,22]. The detector system [Fig. 1(b)] consisted of a fast scintillator (LuAG:Ce, decay time ~50 ns) and a mirror coupled to a high-speed camera (Photron Fastcam SA1.1) via a long-working distance microscope objective (10x with NA = 0.21) [20]. By synchronizing the detector with and gating it to the x-ray pulses, we were able to directly visualize ultrafast evolution dynamics on a μs timescale. Specifically, we took images with a 472 ns exposure time and a 3.68 μs interframe time (corresponding to the storage ring period) [20,22]. The drop-impact

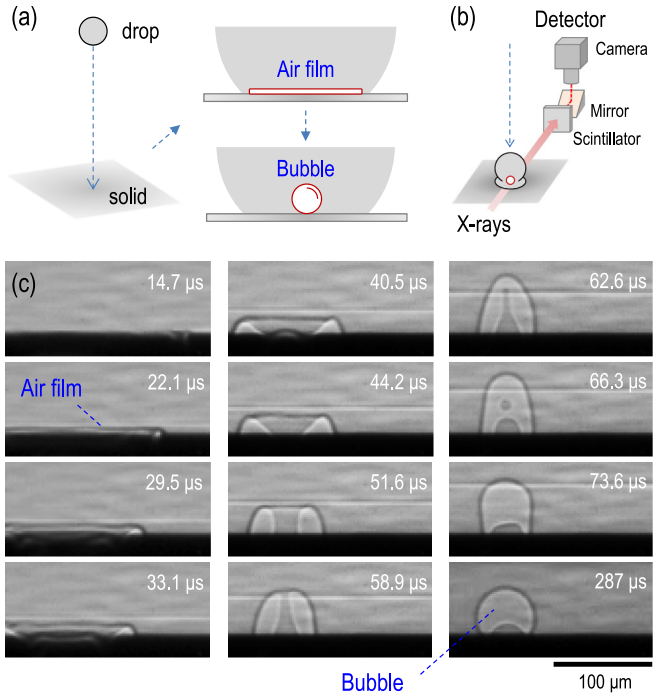

FIG. 1 (color online). Complicated evolution of an air film during drop impact. (a) Schematic description of air film evolution; namely, when an air film is entrapped during drop impact on a solid surface, it should evolve into a bubble to minimize its surface energy. (b) Schematic of ultrafast x-ray phase-contrast imaging, which enables the tracking of dynamic changes of air-liquid interfaces in real time. (c) Representative, sequential x-ray images depicting air film evolution during the impact of a water drop with a diameter of 2.6 mm on an Si wafer from a height of 80 mm. Here the time at the impact moment was set to $t = 0$ (see movie 1 of Supplemental material [25]).

setup was 150 mm from the detector, a distance sufficient to achieve a strong phase-contrast effect. For liquid drops, we used water (surface tension $\sigma_w = 72.75\ \mathrm{mN\,m^{-1}}$, viscosity $\mu_w = 1.005$ mPa s, and density $\rho_w = 996.4\ \mathrm{kg\,m^{-3}}$ at 293 K) and mixtures of water and small amounts of ethanol or glycerol. The drop (diameter $d = 2.6$ mm) was dispensed from a syringe needle (26 G) connected to a remote-controlled syringe pump. The drop was released at a height of 80 mm above the solid surface for all experiments reported here. A laser beam was used to sense the drop and trigger the camera. The drop velocity was $v \sim 1.25\ \mathrm{m\,s^{-1}}$, resulting in a Weber number $\mathrm{We} = \rho v^2 d/\sigma = 55$–$70$ and a Reynolds number $\mathrm{Re} = \rho v d/\mu = 1900$–$3200$. The splashing condition can be defined as $K_d = \mathrm{We}^{1/2}\mathrm{Re}^{1/4} > 57.7$ [2], while our conditions correspond to $K_d = 44$–47. This indicates that our conditions are far from the splashing regime [2,3,18]. A high-speed, mechanical shutter was also installed to restrict the total imaging time to ~10 ms to minimize radiation damage to the scintillator. Hard x-ray irradiation does not significantly affect the properties of liquids in very short exposures (< 300 μs) [24]. A polished silicon wafer (rms roughness <2 nm) was used as a solid substrate and carefully aligned using a high-resolution goniometer.

Figure 1(c) shows representative, sequential images of the evolution of an entrapped air film into a bubble just after the impact of a water drop on a solid substrate. The entrapment of air occurred mainly at $t < 20$ μs, as shown in the first snapshot ($t = 14.7$ μs) (see the corresponding movie 1 [25]), which is consistent with previous results [13]. The radii of the entrapped films at $t < 20$ μs were $R_i \sim 145 \pm 5$ μm, consistent with predicted values [5]. The initial film thickness was ~1 μm ($\approx L^3/6R_i^2$ [18] where L is the final bubble diameter [≈ 50 μm in Fig. 1(c)]), similar to 1.9 μm taken from a range of We ~ 70–900 and Re ~ 1600–5800 [18]. We observed that once the entrapped film is formed at $t < 20$ μs, it retracts very rapidly at $t < 40.5$ μs to minimize its surface energy. During retraction, the upper air surface develops capillary waves. Following retraction ($t > 40.5$ μs), the air volume contracts into a toroidal bubble, which rapidly shrinks until $t = 58.9$ μs. Finally, we found pinch-off of the water that had been confined within the core of the toroidal bubble at $t = 62.6$ μs. The pinch-off process is very important because it generates a tiny secondary (daughter) droplet on the substrate. The daughter droplet has a spherical cap inside the bubble, as observed in the last snapshot ($t = 287$ μs). The evolution of a film to a bubble is depicted schematically in Fig. 2 based on the morphological changes observed in Fig. 1(c). To understand the sequential evolution, it is necessary to analyze each stage.

Retraction.—The radius of the entrapped air, R, was measured as a function of time and is plotted in Fig. 3(a). This system has high Reynolds numbers ($\mathrm{Re} \sim 500$), when taking into account the initial film radius ($R_i \sim 100$ μm) and initial retraction speed ($u_i \sim 5\ \mathrm{m\,s^{-1}}$), indicating that the retraction is governed by competition between the surface tension σ and the inertia (thus, "inertial retraction") [18]. The inertial retraction is apparent

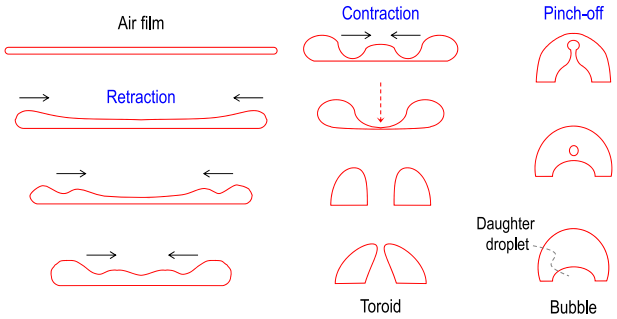

FIG. 2 (color online). Schematic of the complicated air film evolution process during drop impact: inertial retraction of an air film, contraction of the top air surface into a toroid bubble, and pinch-off of a daughter droplet in the bubble. The solid-line arrows denote the propagation of capillary waves, and the dashed-line arrow indicates the contact between the crest and the substrate.

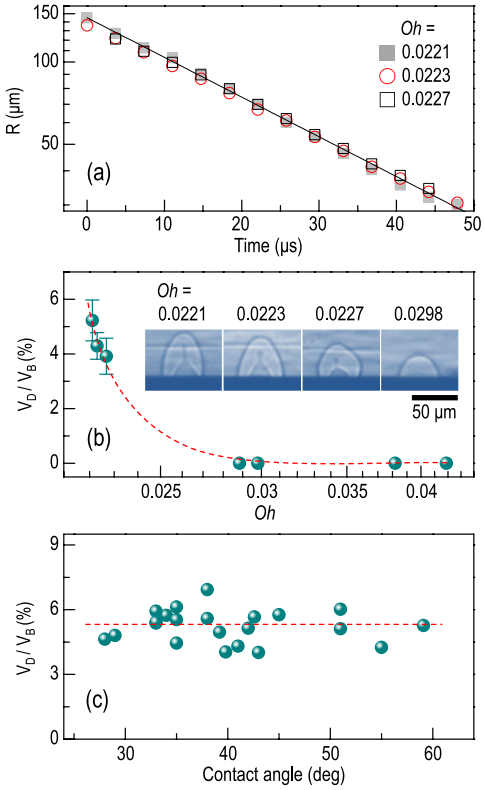

FIG. 3 (color online). Detailed dynamics of air film evolution. (a) The radius of the air film (R) was measured as a function of time (t) during retraction for different liquids (characterized by Oh: 0.0221 for water and 0.0223 and 0.0227 for two different mixtures of water and ethanol). There is an exponential decrease in R over time, fitted by $R(t) = (1.45 \times 10^{-4}) \exp(-3.34 \times 10^{4} t)$ (solid line) for water, which indicates inertial retraction based on the film thickening [18]. (b) The ratio of the daughter droplet volume to the air bubble volume, V_D/V_B, was evaluated with Oh. The data support the existence of a critical Oh (Oh^*) above which the pinch-off of the daughter droplet is prevented. The inset shows the x-ray images of the pinch-off moments in different liquids. (c) The volume fraction, V_D/V_B, for water is almost invariant with the substrate contact angle at $\sim$5.2% ($\pm$ 0.7%). The dashed lines are guides for the eye. These results suggest that the energy transfer, expressed in terms of Oh, is essential for the daughter droplet generation.

with the exponential decrease of R over time, described as [18,26]

$$R(t) = R_i \exp(-C\sqrt{\pi\sigma/\rho V}t),$$

where ρ is the density of the liquid, V is the total volume of air, and C is a proportionality constant. By fitting the R-t data and inserting the parameter values, C is given as $\sim$0.69 for $d = 2.6$ mm. This is consistent with Ref. [18] where $C = 0.88$ for $d = 4$ mm and C is proportional to $d^{1/4}$. The retraction speed decreases exponentially with time, given by $u = dR/dt \sim -(\sigma/\rho\delta)^{1/2}$, where the air film thickness δ increases with time [18,26]. The inertial retraction and its decrease in speed influence subsequent stages.

Contraction and pinch-off.—Contraction and pinch-off rely on energy transfer through capillary waves during the retraction. The capillary waves are generated at the film edge by the energy coming from the impact, as shown in Fig. 1(c) (between $t = 22.1$ and 40.5 μs) and illustrated in Fig. 2 (solid-line arrows). The propagation speed of the waves was 4.2 ± 0.2 m s^{-1}, which is consistent with the estimated group velocity of $1.5(2\pi\sigma/\rho\lambda)^{1/2} \sim 4.1$ m s^{-1} [18] calculated from the measured wavelength $\lambda \sim 60 \pm 5$ μm ($\lambda \ll d/2$; d = the drop diameter). This speed is slightly faster than that for a different impact condition with We = 34 and Re = 4200 [18]. It is important to note that the propagation speed exceeds the retraction speed after $t > 20$ μs [Fig. 3(a)]. As a result, the capillary waves converge at the center, and their crests touch the substrate [44.2 μs in Fig. 1(c) and dashed-line arrow in Fig. 2], as proposed previously [18]. This leads to *contraction* of the air film, resulting in a toroidal bubble (Fig. 2). Here, the contact area of the liquid confined in the toroid core on the substrate shows little variation, which is attributed to the adhesion of the liquid on the substrate. Therefore, it is conceivable that the minimization of the surface energy would promote *pinch-off* of the liquid (Fig. 2). We occasionally observed the emission of free satellite droplets [66.3 μs in Fig. 1(c)], similar to liquid jetting [22].

Energy transfer can be understood with the *Ohnesorge* number, $\mathrm{Oh} = \mu/(\rho\sigma R_B)^{1/2}$, a hydrodynamic number that indicates a balance between viscous damping and capillary force [22,27], where R_B is the radius of the final spherical bubble. The energy coming from the impact is transferred through capillary waves along the air-liquid free surface and the liquid viscosity hinders the energy transfer. In this study, Oh was controlled from 0.022 to 0.045 by adding a small amount of ethanol or glycerol to the water. Figure 3(b) shows the Oh dependence of the ratio of the daughter droplet volume (V_D) to the air bubble volume (V_B); V_D/V_B decreases with Oh. The daughter droplet is only generated at $\mathrm{Oh} \leq 0.0227$, with no daughter droplets forming at $\mathrm{Oh} \geq 0.0288$. Here, the retraction dynamics were identical at $\mathrm{Oh} \leq 0.0227$ [Fig. 3(a)]. These data provide evidence that at high Oh values, viscous damping weakens the capillary waves, possibly resulting in a reduction of the mass transport, which explains the decrease in V_D/V_B with increasing Oh. This result suggests the existence of a critical Oh value (Oh^*) above which viscous damping prevents pinch-off of the daughter droplet. Interestingly, the measured value of $\mathrm{Oh}^* \sim 0.026 \pm 0.003$ [Fig. 3(b)] is comparable to the Oh^* value ($\sim$0.026) corresponding to the partial coalescence of liquid drops [27]. This result implies that the physics of daughter droplet generation is analogous to that of liquid coalescence.

The above result suggests that daughter droplet generation depends primarily on the Oh values. We tested the influence of surface wettability on daughter droplet generation at a fixed Oh = 0.0221. Figure 3(c) shows the invariance of V_D/V_B with the surface contact angle, which was modified by x-ray irradiation [24,28]; namely, V_D/V_B is almost constant at ~5.2% (± 0.7%). This result clearly indicates that surface wettability is irrelevant to daughter droplet generation in terms of Oh. Additionally, surface wettability does not affect the spreading of the daughter droplet [29,30] at very short time scales (~ 10 μs) during the contraction [Fig. 1(c)], which is one of the reasons for the invariance of V_D/V_B.

Bubble detachment.—Although the surface wettability does not affect the spreading of the daughter droplet, it does affect the adhesion of the bubble on the substrate [16,18]. We found that the resultant bubble detached from the substrate when the contact angle θ was relatively small, for instance, at $\theta = 35°$, as shown in Fig. 4(a) (arrows). Otherwise, the bubble remained adhered to the substrate at relatively high contact angles, such as $\theta = 45°$ [Fig. 4(b)] and $\theta = 50°$ [Fig. 1(c)]. Figure 4(c) shows the frequency of bubble detachment and attachment as a function of contact angle. The threshold contact angle (θth) is ~40 ± 5°, below which the bubble detached. This result indicates that surface wettability is critical to bubble detachment.

In this section, we discuss why wettable substrates are favorable for bubble detachment. At small contact angles [Fig. 4(d); upper], the daughter droplet (marked by "D") spreads out, merges with the "mother drop" (marked by "M"), and finally separates the bubble from the substrate. At large contact angles, the droplet tends to stay inside the bubble [Fig. 4(d); bottom], leading to bubble attachment. The threshold angle θth is ~42.5°, based on the geometric constraints: (i) spherical cap models (V_D depends only on θ at a fixed R_D and $\theta_B = \theta_D = \theta$ where the subscripts B and D denote the bubble and the daughter droplet, respectively) [31,32], (ii) $R_D \geq R_B$ (as the detachment condition), and (iii) $V_D/V_B \sim 0.052$ for water [Fig. 3(c)]. This estimate is comparable to our measurement of θth ~ 40 ± 5° [Fig. 4(c)]. This mechanism provides a good explanation of bubble detachment on wettable substrates. The pinch-off and spreading of the daughter droplet may occur asymmetrically, but bubble attachment can be maintained despite one-sided merging [Fig. 4(b); arrows]. Finally, we expect that because V_D/V_B depends on Oh, the threshold contact angle may decrease if Oh increases. Indeed, no detachment was found at 40° at a large Oh > 0.0223. The influence of the substrate wettability would be useful as a way to eliminate bubbles by reducing the contact angle during drop impact in many applications, such as ink-jet printing, spray coating, and metal casting [15–18,33].

In summary, we used ultrafast x-ray phase-contrast imaging to determine that the evolution of an air film to a bubble occurs through a complicated, sequential process. The sequential evolution consists of three stages: inertial retraction of the air film, contraction of the top air surface into a bubble, and pinch-off of a daughter droplet in the bubble. The generation of the daughter droplet inside the bubble is explained by the critical Oh number, and the subsequent detachment of the bubble is explained by the threshold contact angle. Bubble detachment may be a feasible way to eliminate bubbles in many drop-impact applications.

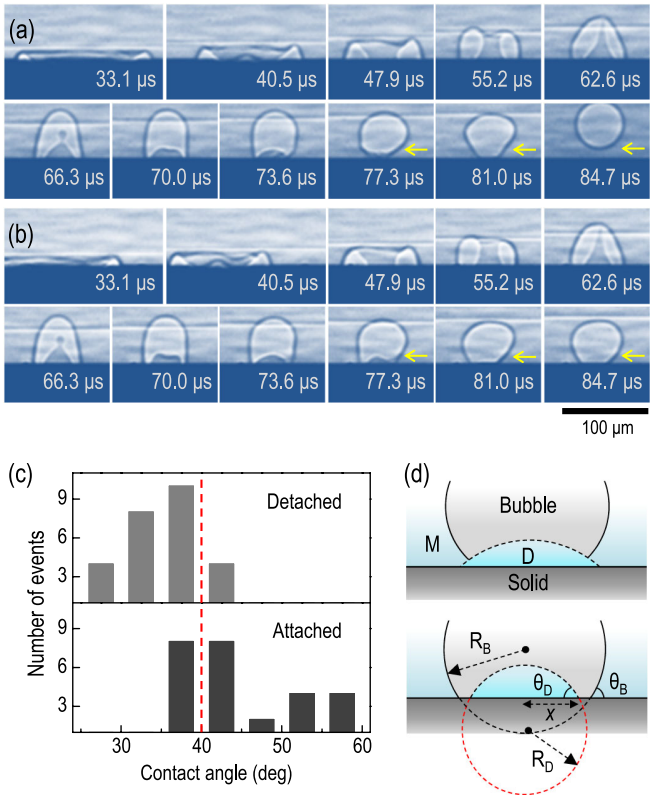

FIG. 4 (color online). Bubble detachment and attachment. Sequential x-ray images for water clearly show examples of (a) bubble detachment at a contact angle ~35° and (b) bubble attachment at ~45° (see movies 2 and 3 of Supplemental material [25]). A critical difference in bubble behavior was found after 77.3 μs (marked by arrows). (c) The frequency of bubble detachment and attachment for water was monitored as a function of the substrate contact angle; the threshold contact angle was ~40 ± 5°, below which the bubble preferably detached. (d) The detachment (upper, for small contact angles) and attachment (lower, for large contact angles) can be explained by geometrical relations, which suggest ~42.5° to be the threshold angle, comparable to our measurements of (c).

This research was supported by the Creative Research Initiatives (Functional X-ray Imaging) of MEST/NRF. Use of the Advanced Photon Source, an Office of Science User Facility operated for the DOE Office of Science by Argonne National Laboratory, was supported by the U.S. DOE under Contract No. DE-AC02-06CH11357.

*bmweon@hotmail.com
†jhje@postech.ac.kr

[1] M. Rein, Fluid Dyn. Res. **12**, 61 (1993).
[2] A. L. Yarin, Annu. Rev. Fluid Mech. **38**, 159 (2006).
[3] L. Xu, W. W. Zhang, and S. R. Nagel, Phys. Rev. Lett. **94**, 184505 (2005).
[4] S. Mandre, M. Mani, and M. P. Brenner, Phys. Rev. Lett. **102**, 134502 (2009).
[5] M. Mani, S. Mandre, and M. P. Brenner, J. Fluid Mech. **647**, 163 (2010).
[6] P. D. Hicks and R. Purvis, J. Fluid Mech. **649**, 135 (2010).
[7] M. M. Driscoll, C. S. Stevens, and S. R. Nagel, Phys. Rev. E **82**, 036302 (2010).
[8] S. T. Thoroddsen, M.-J. Thoraval, K. Takehara, and T. G. Etoh, Phys. Rev. Lett. **106**, 034501 (2011).
[9] L. Duchemin and C. Josserand, Phys. Fluids **23**, 091701 (2011).
[10] M. M. Driscoll and S. R. Nagel, Phys. Rev. Lett. **107**, 154502 (2011).
[11] R. C. A. van der Veen, T. Tran, D. Lohse, and C. Sun, Phys. Rev. E **85**, 026315 (2012).
[12] J. M. Kolinski, S. M. Rubinstein, S. Mandre, M. P. Brenner, D. A. Weitz, and L. Mahadevan, Phys. Rev. Lett. **108**, 074503 (2012).
[13] J. de Ruiter, J. M. Oh, D. van den Ende, and F. Mugele, Phys. Rev. Lett. **108**, 074505 (2012).
[14] A. Latka, A. Strandburg-Peshkin, M. M. Driscoll, C. S. Stevens, and S. R. Nagel, Phys. Rev. Lett. **109**, 054501 (2012).
[15] S. Chandra and C. T. Avedisian, Proc. R. Soc. A **432**, 13 (1991).
[16] V. Mehdi-Nejad, J. Mostaghimi, and S. Chandra, Phys. Fluids **15**, 173 (2003).
[17] D. B. van Dam and C. Le Clerc, Phys. Fluids **16**, 3403 (2004).
[18] S. T. Thoroddsen, T. G. Etoh, K. Takehara, N. Ootsuka, and Y. Hatsuki, J. Fluid Mech. **545**, 203 (2005).
[19] S. W. Wilkins, T. E. Gureyev, D. Gao, A. Pogany, and A. W. Stevenson, Nature (London) **384**, 335 (1996).
[20] K. Fezzaa and Y. Wang, Phys. Rev. Lett. **100**, 104501 (2008).
[21] L. V. Zhang, J. Toole, K. Fezzaa, and R. D. Deegan, J. Fluid Mech. **690**, 5 (2012).
[22] J. S. Lee, B. M. Weon, S. J. Park, J. H. Je, K. Fezzaa, and W.-K. Lee, Nature Commun. **2**, 367 (2011).
[23] B. M. Weon and J. H. Je, Phys. Rev. Lett. **108**, 224501 (2012).
[24] B. M. Weon, J. H. Je, Y. Hwu, and G. Margaritondo, Phys. Rev. Lett. **100**, 217403 (2008).
[25] See Supplemental Material at http://link.aps.org/supplemental/10.1103/PhysRevLett.109.204501 for the x-ray movies of representative air film evolution to a bubble (movie 1) and for the cases of bubble detachment (movie 2) and of bubble attachment (movie 3).
[26] S. T. Thoroddsen, T. G. Etoh, and K. Takehara, J. Fluid Mech. **478**, 125 (2003).
[27] F. Blanchette and T. P. Bigioni, Nat. Phys. **2**, 254 (2006).
[28] Y. B. Kwon, B. M. Weon, K. H. Won, J. H. Je, Y. Hwu, and G. Margaritondo, Langmuir **25**, 1927 (2009).
[29] J. C. Bird, S. Mandre, and H. A. Stone, Phys. Rev. Lett. **100**, 234501 (2008).
[30] S. C. Case and S. R. Nagel, Phys. Rev. Lett. **100**, 084503 (2008).
[31] J. Drelich, J. D. Miller, and R. J. Good, J. Colloid Interface Sci. **179**, 37 (1996).
[32] M. Taylor, A. J. Urquhart, M. Zelzer, M. C. Davies, and M. R. Alexander, Langmuir **23**, 6875 (2007).
[33] J. Campbell, *Castings: The New Metallurgy of Cast Metals* (Butterworth Heinemann, Burlington, 2003).